Accuracy assessment of a Lucas-Kanade based correlation method for 3D PIV

A. Cheminet, B. Leclaire, F. Champagnat, A. Plyer, R. Yegavian, G. Le Besnerais

Accuracy assessment of a Lucas-Kanade based correlation method for 3D PIV

Adam Cheminet[1*], Benjamin Leclaire[1], Frédéric Champagnat[2], Aurélien Plyer[2], Robin Yegavian[1] and Guy Le Besnerais[2]

1: DAFE/ONERA, 8 rue des Vertugadins, 92190 Meudon, FRANCE
2: DTIM/ONERA, chemin de la Hunière, 91761 Palaiseau cedex, FRANCE
* correspondent author: adam.cheminet@onera.fr

Abstract. We introduce and characterize a new 3D cross-correlation algorithm, which relies on gradient-based iterative volume deformation. The algorithm, FOLKI3D, is the extension to 3D PIV of the approach introduced by Champagnat et al. 2011. It has a highly parallel structure and is implemented on GPU. Additionally to the gradient approach for displacement estimation, we implemented a high-order interpolation scheme (with cubic B-Splines) in the volume deformation step, at a reasonable computational cost. Performance tests on synthetic volumic distributions first allow to characterize the spatial transfer function of the algorithm, and to confirm the efficiency of this interpolator, comparable to that of standard image deformation methods in planar PIV. A second series of synthetic tests then investigates the response of FOLKI3D to sources of noise specific to the tomographic PIV context, i.e. ghost particles. Depending on the tests, the algorithm is found as efficient or more robust than the state-of-the-art. The gain brought by the high-order interpolation is also confirmed in a situation with a large number of ghosts, and different reconstructed particle shapes.

1. Introduction

Tomographic PIV offers a tremendous potential for the characterization of complex flows, as it enables the instantaneous measurement of three-dimensional velocity fields. This gain in capacity comes however with new questions and challenges. In terms of accuracy, much effort has been devoted to characterizing the specific noise introduced by the reconstruction step, which is specific to the 3D context and may have a significant impact on the final result. Many researchers have also directed their work towards reducing the problem complexity (see, e.g., Scarano 2013, for a review on both these points). Indeed, handling 3D volumes represents a huge amount of data, and thus potentially prohibitive processing times. This may also constrain algorithmic choices, as approaches, which were proven successful and accurate in 2D PIV, may be prohibitive in 3D with the current computational capacities.

In this paper, we propose a new approach for 3D cross-correlation, consisting in a gradient-based iterative volume deformation method, in the Lucas-Kanade framework. It is the extension to 3D of the approach proposed in Champagnat et al. 2011 and, due to its highly parallel structure, is also implemented on GPU. Volume deformation may be performed with a simple, linear interpolation as in most algorithms, or, thanks to an efficient implementation, with a higher-order, cubic B-Spline scheme, while maintaining reasonable processing times. Our purpose in this paper will be to characterize this algorithm, with a particular emphasis on its response to specific 3D noise sources. Focus will also be placed on the possible gains arising from high-order interpolation in this context.

The paper is structured as follows. First, we recall the principle of the method, with an emphasis on the useful parameters and their influence. We then use synthetic tests to characterize the algorithm in terms of spatial resolution and to assess the impact of the interpolation scheme on bias and rms errors in the subvoxel displacement estimation. Finally, we assess the algorithm's robustness to noise, especially tomographic PIV noise, ie ghost particles, by using synthetic simulations of 3D tomographic PIV experiments.

2. General principle

The present implementation is the extension to 3D of the algorithm FOLKI-PIV, described in Champagnat et al. (2011). We thus present here the main characteristics only and refer the reader to this paper for more detail.

2.1. Iterative scheme

Considering a discretized physical volume, let k denote the index of a voxel in the grid. As in traditional correlation-based PIV, our objective is to determine the displacement u(k) of a particle pattern contained in the interrogation volume (IV), V(k) centered around voxel k. The mathematical objective however differs and belongs to the Lucas-Kanade paradigm (see Baker and Mathews, 2004, for a review), as it amounts to minimize the sum of squared differences (SSD).

$$u(k) = \arg\min \sum_m v(m-k)\left(E_1\left(m - \frac{u(k)}{2}\right) - E_2\left(m + \frac{u(k)}{2}\right)\right)^2 \quad (1)$$

Here E_1 and E_2 respectively denote the volume intensity distributions reconstructed at the illumination instants t and t+dt, and function v is the support of interrogation volume V(k). Note that this criterion is symmetrical, i.e. it leads to a second order estimate of u(k) in time, at t+dt/2. In practice, we use either a top-hat cubic IV, parameterized by its radius R, or a Gaussian cubic IV, defined by two parameters: the radius R and its standard deviation σ.

Minimization of (1) is performed using Gauss-Newton (GN) iterations. Supposing that a predictor $u_0(k)$ is available, one then replaces u(k) by u(k) - u_0(m) + u_0(m), so that

$$u(k) = \arg\min \sum_m v(m-k)\left(E_1^{-u_0/2}\left(m - \frac{u(k)-u_0(m)}{2}\right) - E_2^{u_0/2}\left(m + \frac{u(k)-u_0(m)}{2}\right)\right)^2 \quad (2)$$

Here, one has introduced the deformed (or warped) intensity distributions

$$\begin{cases} E_1^{-u_0/2}(m) = E_1\left(m - \dfrac{u_0(m)}{2}\right) \\ E_2^{u_0/2}(m) = E_2\left(m + \dfrac{u_0(m)}{2}\right) \end{cases} \quad (3)$$

The following step then consists in linearizing (2), assuming that the displacement increment to be found is weak, i.e. u(k) - u_0(m) ≈ 0, so that

$$u(k) = \arg\min \sum_m v(m-k)\left(E_1^{-u_0/2}(m) - E_2^{u_0/2}(m) - \frac{\nabla E_1^{-u_0/2}(m) + \nabla E_2^{u_0/2}(m)}{2}\left(u(k)-u_0(m)\right)\right)^2 \quad (4)$$

Finally, after some algebra, deriving the SSD in (3) leads to finding u(k) as the solution of a 3x3 linear system

$$H(k)u(k) = c(k) \quad (5)$$

where matrix H and left-hand-side c involve the predictor u_0, the deformed volumes, and their gradients.

2.2. Processing flow-chart and control parameters

Similarly to the plane approach of FOLKI-PIV, the guess-value is obtained by implementing a multi-resolution Gaussian pyramid of intensity volumes. A pyramid contains J levels, including the raw intensity volume (level 0). Level j+1 is formed by applying a low-pass filter on level j, and then retaining one pixel out of a cube of 2x2x2 voxels. Thus, volumes at level j+1 are eight times smaller than at level j, and displacements are divided by two in each direction. The number of levels J has then to be chosen according to the maximum displacement expected. Indeed, a condition for the GN iterations (4) to converge is that the predictor be close to the exact displacement. Considering enough levels will thus allow this convergence when choosing a zero displacement field as the predictor for level J-1. GN iterations are then run at this level until convergence. The final estimate is interpolated at level J-2 and serves as the first predictor for the GN iterations at this level. The process is then repeated until convergence is reached at level 0.

To ensure robustness with respect to variations in intensity in the volumes, a mean and standard deviation normalization is applied at each pyramid level prior to the GN iterations (see Champagnat et al. 2011 for more details). Also, similarly to FOLKI-PIV, FOLKI3D produces a dense output (one displacement per voxel) with no computational overload, while its resolution remains tied to the IV size (see the tests below).
To sum up, FOLKI3D is tuned by three main parameters:

- The number J of pyramid levels, which depends on the maximum displacement expected in the volumes
- The number N of GN iterations performed at each level. Usually, 3 to 10 iterations are enough to reach convergence, the exact number usually depending on the signal-to-noise ratio of the volumes
- The size of the interrogation volume, which controls the spatial resolution of the result, as in traditional cross-correlation PIV, and will be shown below.

2.3. Comments

One of the PIV algorithms currently acknowledged as a state-of-the art in the literature is an iterative image or volume deformation method (IDM), whether the estimation is done on planar or volumic data (see, for instance, Scarano, 2002 and Scarano, 2013). In a 3D framework, supposing that a predictor displacement field is available, the 3D intensity fields are first deformed with this displacement value, requiring a subvoxel interpolation scheme. Then the subvoxel increment allowing to maximize the cross-correlation from these deformed volumes is determined, by using a three-point Gaussian fit. This results in a new estimate of the displacement. As pointed out by several authors in the literature, it is necessary to smooth this displacement field in order to prevent a divergence of the iterative scheme; choosing an adapted filter kernel may also enable to improve the algorithm transfer function, as studied in detail by Schrijer & Scarano (2008). Once this filtering is done, the data may be used again for deformation, and so forth.

Though FOLKI3D belongs to a Lucas-Kanade paradigm, it also belongs to the IDM family, with similarities to the above described flow-chart. Firstly, the global objective, formulated as the minimization of a Sum of Squared Differences (1), becomes identical to maximizing a Cross-Correlation score as soon as the mean and standard deviation pre-processing is performed. When transposed in an iterative context, FOLKI3D also uses volume deformation at the subvoxel level before each iteration, as shown by equations (2) and (3). The following steps however differ from traditional IDM algorithms: indeed, instead of computing the whole cross-correlation map on a given domain by FFT or direct correlation, and then refining the maximum by a Gaussian fit, FOLKI3D determines the minimum of the SSD iteratively using a gradient method, directly at a subvoxel level. Also, as described in Leclaire et al. (2011), the displacement increment is defined in a slightly different way as in traditional IDM algorithms, which guarantees stability with the number of iterations and makes the intermediate filtering step of the displacement before deformation unnecessary.

The next section will present the response of FOLKI3D to traditional tests used in the literature, which will enable to further situate it among the IDM framework.

3. Spatial resolution and interpolation schemes

In this section, we introduce a first series of synthetic tests to assess the performances of FOLKI3D. This is done on ideal 3D blob-like particle distributions (i.e. supposing ideal tomographic reconstructions), in order to determine the spatial resolution of the algorithm, and the influence of the interpolator choice on the bias and random errors.

3.1. Spatial wavelength response

Following Scarano and Riethmuller (2000) the frequency response of a PIV algorithm can be evaluated using a sinusoidal shear displacement test :

$$(U,V,W)=\left(A\sin(2\pi\frac{Y}{\lambda}),0,0\right) \quad (6)$$

where X,Y and Z are the 3D coordinates and U,V,W the associated displacement components. For this test, 3D ideal particles randomly distributed in the correlation volume, are generated by locally expanding a physical point particle to a 3D Gaussian blob with $\sigma = 0.6$ voxel (thus a diameter of 2.4 voxel), in order to have a volumetric distribution well adapted to the correlation algorithm. The particle density is high compared to real tomo PIV experiments densities, in order to have at least 20 to 30 particles per IV for the smaller IV size. We then use this displacement field (6) with amplitude A set to 2 voxels and the wavelength λ varied from 20 to 400 voxels. FOLKI3D interrogation volume (IV) size is varied from 11 to 63 voxels. As the displacement is rather close to zero, we use J=1 level and N=3 iterations. B-Spline interpolation scheme was used for the volume deformation step. For each volume corresponding to a given (λ,R) couple, we compute the ratio between the estimated amplitude of the sinusoid $A_{FOLKI-3D}$ and the ground truth value A=2 voxels. The evolution of this ratio as a function of the normalized IV size $2R/\lambda$ is plotted in Fig 1. In **Fig. 1** (left) we used a cubic top-hat interrogation volume, and in **Fig. 1** (right) we used Gaussian IVs with a given σ/R ratio. In **Fig. 1** (left), all values of $A_{FOLKI-3D}/A$ nearly collapse on a cardinal sine curve, which is the frequency response to a [-R,R] sliding average, as usually in correlation based methods (Scarano and Riethmuller, 2000). In particular, this means that the spatial resolution of FOLKI3D is, as well, directly linked to the size of the IV. The fact that a dense output (one vector per voxel) is obtained is an algorithmic specificity, and retaining all voxels in the final results would correspond to over-sampling.

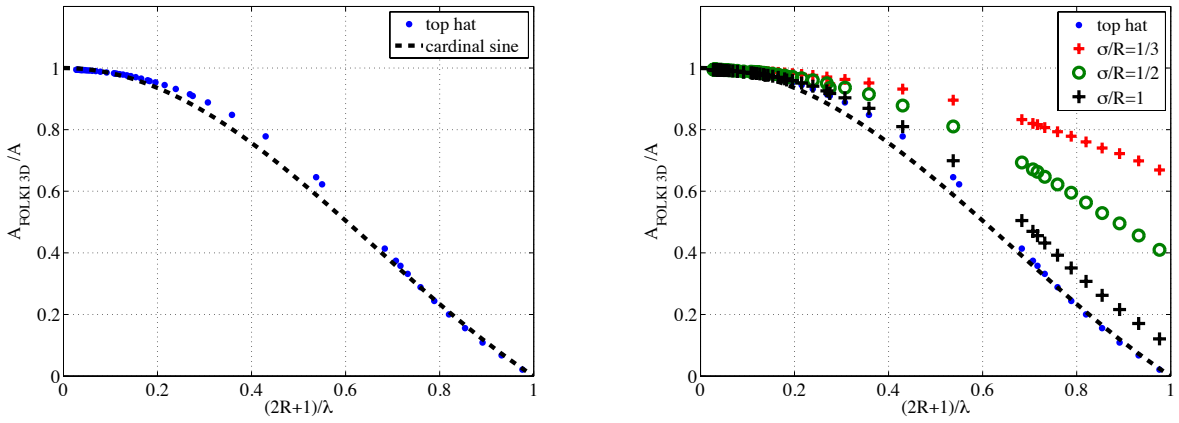

Fig. 1 Amplitude ratio $A_{FOLKI-3D/A}$ as a function of the normalized volume interrogation size for (left) top hat IVs and (right) Gaussian IVs. The dashed line is the response of a [-R,R] sliding average (cardinal sine function)

3.2. Interpolation schemes and Peak-locking

It is known from several studies on planar PIV that the choice of the interpolation scheme used to deform the images may have an important effect on the displacement precision at a subpixel level. This has been studied in detail by Astarita & Cardone (2005), in particular. In their work, an important number of schemes is introduced, and the accuracy is logically found to be inversely linked to the computational cost of the interpolator, i.e. the cheaper the interpolator (e.g., linear), the less precise the result. As the performance of the algorithms and hardware has evolved rapidly, some of the advanced interpolation methods (such as with cubic B-Splines, or even more precise using a cardinal sine basis) are now commonly used in planar PIV. In the 3D context however, domain sizes are much larger so that the question of using more advanced interpolation schemes than the linear one may come with a dramatic increase of the computational cost. Thus, as mentioned by Scarano (2013), linear interpolation remains the standard.

Building on optimizations begun during works on planar PIV (Champagnat et al. 2011), Champagnat & Le Sant (2013) recently proposed an implementation for cubic B-Spline interpolation which is particularly optimized for GPU, and may be used in FOLKI3D. In practice, this optimization guarantees that the increase in computational time compared to linear interpolation remains reasonable, with a significative increase in accuracy. As in section 3.1, we consider perfect volumic blob-like synthetic distributions. In **Fig. 2**, we monitor the bias and rms error for increasing values of a unidimensional displacement (U,0,0), with U ranging from 0 to 2 voxels, and the standard deviation of the Gaussian blob set to $\sigma = 0.625$ (2.5 voxel wide blob). As shown in Astarita and Cardone (2005), for symmetric IDM algorithms such as FOLKI3D, this range is sufficient to explore, as the response is periodic. Note that we chose the seeding density so as to have the same number of tracers in an IV as the number of particles in the IWs chosen by Astarita and Cardone (ie of the order of 20).

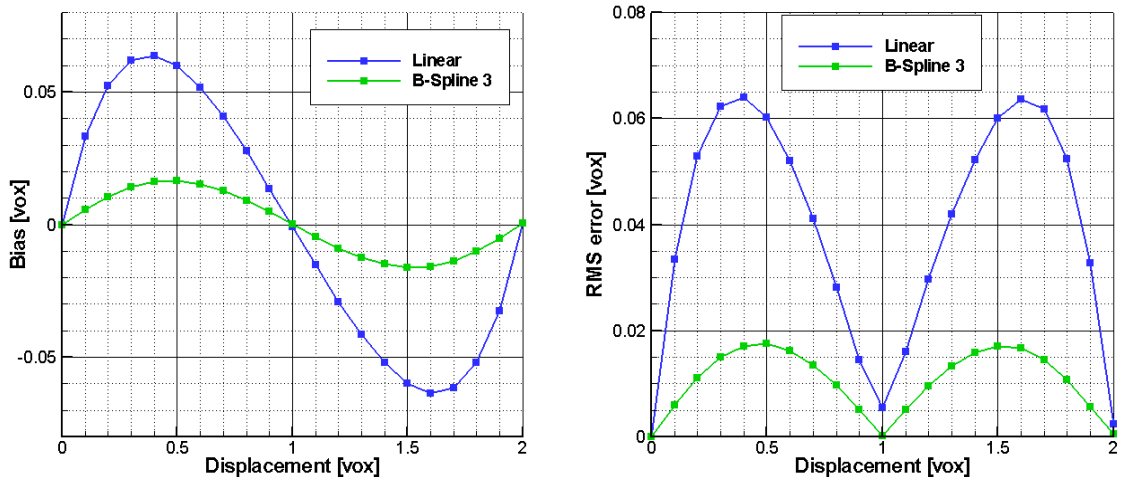

Fig. 2 Bias (left) and rms error (right) for both linear and cubic B-Spline interpolators, for increasing values of the uni-directional displacement (U,0,0).

When using a cubic B-Spline interpolation, the maximum bias error for this particle size is roughly equal to 0.017 voxel, compared to 0.064 for the linear scheme (gain of a factor larger than three). This gain is similar in terms of maximum rms error, with respectively 0.018 and 0.064 voxel. These curves and their maxima are in excellent agreement with the results of Astarita and Cardone (2005), confirming the similarity of FOLKI3D with standard IDM algorithms. The slight differences observed may stem from the fact that we consider a monodisperse seeding, whereas Astarita and Cardone allowed a variation of the particle diameter in their images, and also from the difference in the final subvoxel/pixel estimation (i.e. minimization vs. Gaussian fit, see section 2.3)

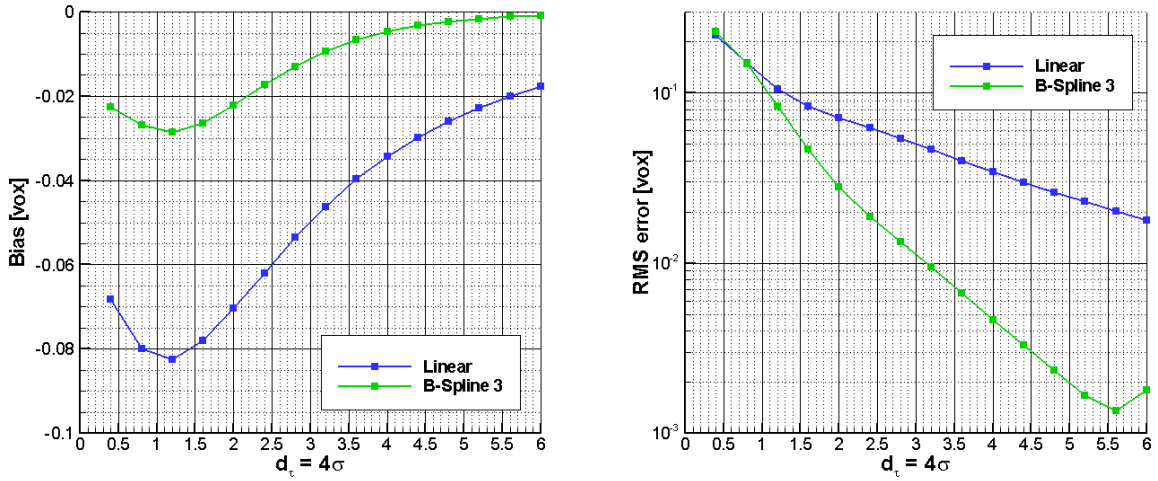

Fig. 3 Bias (left) and rms error (right) for both linear and cubic B-Spline interpolators as a function of the 3D particle diameter d_τ, for a displacement (U,V,W) = (1.5,0,0) voxel.

As the shape and size of the particles produced by the tomographic reconstruction depend from the size of their image on the camera sensors, but also of the geometrical arrangement, it is even more important than in plane PIV to assess the accuracy of the algorithm to different particle sizes. This is done in **Fig. 3** , where the plots represent the bias and rms errors corresponding to a uniform displacement (U,V,W) = (1.5,0,0) (for which the rms error is maximum, see **Fig. 2**), for varying values of the particle diameter $d_\tau = 4\sigma$. Here again, results are in very good agreement with those of Astarita and Cardone, with a systematic reduction in bias, and a quasi-systematic reduction in rms error, for the B-Spline scheme. The gain in rms error increases with increasing particle diameter. Note that, compared to Astarita and Cardone, the B-Spline scheme of FOLKI3D is slightly less efficient for very small particles compared to the linear scheme. However, the minimum level of rms error reached with the B-Spline scheme is smaller. As the synthetic conditions should be close to identical between our study and that of Astarita and Cardone for this second test, these differences are most likely ascribed to the subpixel estimation approach.

4. Robustness versus Tomographic 3D noise

We now turn to more realistic conditions, using the complete 3D PIV setup, and tomographic reconstructions. Our objective in this section is to assess the robustness of the algorithm to specific noise sources encountered in the 3D framework, i.e. to the influence of various effects linked to the presence of ghost particles.

Similar to traditional sources of noise in planar PIV, the ghost particles play a key role in the accuracy of the result, and in the choice of the experimental parameters (see, for instance, Elsinga et al. 2006). Indeed, the number of ghosts is known to increase with seeding density, whereas the accuracy of motion estimation increases with seeding density. Thus, additionally as increasing the rms error, they also play a key role in the spatial resolution of the result, as the choice of the IV size has to result from a trade-off between spatial resolution (small IV, requiring a high seeding) and noise (which decreases when the IV size increases). Besides, as shown by Elsinga et al. (2011), depending on the setup and displacement field, a proportion of ghosts may be coherent between the two laser pulses, thereby adding a bias to the result.

In the following, we will assess the response of FOLKI3D to these sources of noise and bias, and, for some of them, compare it to the state-of-the-art, using LaVision Davis 8.2 software. Additionally to the bias due to coherent ghosts, we will also consider the influence of viewing conditions, and, in that respect, assess the differences obtained for the two interpolation schemes of FOLKI3D. These conditions may play a significant role; firstly, Cheminet et al. (2013) and Cornic et al. (2013) recently showed that the ratio between the intersection and the union of the camera fields of view directly influences the proportion of ghosts, whereas

it is also known that different directions result in different shapes of the reconstructed particles, as for instance summed up in Scarano (2013).

4.1. Tomographic synthetic setup

3D particle distributions reconstructed from PIV images are generated from a classical 3D Tomographic PIV setup. Our simulations involve four cameras, which are positioned on a single side of a laser volume. Their positions depend on the tests and will be addressed further down in this paper. A pinhole model is assumed for the cameras, without Scheimpflug adapter for simplicity, and calibration is supposed to be perfectly known and to obey a pinhole model. The focal length is 100 mm, thus the magnification factor M is equal to 0.1, and the pixel size is 10 µm with a fill factor of 100%.

The laser sheet is modeled as a 20 mm thick parallelepiped. Its intensity profile is assumed to be uniform. The reconstructed volume, also 20 mm thick, is taken as the smallest parallelepiped including the illuminated volume seen by all the cameras. Thus it depends on the field of view and is given for each experiment. The voxel-to-pixel ratio is in this paper always set to one. We use 512x512 pixels cameras, which lead to typical reconstruction sizes of the order of 600x600x200 voxels. Unless otherwise specified, the cameras are positioned on a single side of the laser sheet at the vertices $(\frac{\pm 1}{2}, \frac{\pm 1}{2}, \frac{1}{\sqrt{2}})$ of a square of 1 meter side. They are positioned at 1 meter from the centre of the reconstructed volume located at (0,0,0) and point at it.

Tracers particles are uniformly distributed in the light sheet volume. The density is controlled by the particle per voxel count (ppv) and is set such that the particle density image (Nppp) is equal to 0.056. Horizontal and vertical extension of the laser sheet are larger than the field of view covered by all the cameras. Thus all illuminated particles cannot be seen by all cameras, a fact that always occurs in real datasets and is however often overlooked in synthetic experiments (Cheminet et al., Cornic et al. 2013). Unless otherwise specified, the illuminated particles lie in the union of the laser sheet and the cameras fields on view (Union) and the reconstruction process is done on the intersection of those volumes (Intersection). For simplicity the scattered light is taken as uniform and we will consider a monodisperse seeding.

Considering P particles with intensity E_p located at point X_p in 3D-space, the intensity distribution in the image is given by :

$$I(\boldsymbol{x}) = \sum_{p=1}^{P} E_p . h(\boldsymbol{x} - F(\boldsymbol{X_p})) \quad (7)$$

where x=(x,y) denotes any location in the image plane, F is the geometric projection function in the image, and h the so-called Point Spread Function (PSF), which models the aperture limited diffraction and pixel integration. For the tests presented in this paper, we assume a Gaussian PSF with standard deviation σ_{psf} set to 0.6, with a 100% fill factor. We assume an image dynamic range of 8 bit, and a Gaussian noise with mean=0 and standard deviation 2 is added to the images. Its amplitude is set at about 10% relative to the maximum particle intensity.

Tomographic reconstruction is then performed using an MLOS-SMART algorithm similar to that of Atkinson and Soria (2009), with 25 iterations and the relaxation parameter µ set to 1.

4.2. Robustness versus coherent ghost particles

4.2.1. Displacement field

Elsinga et al. (2011) showed that under certain conditions displacement errors arise due to the coherent motion of ghost particles. This occurs when a given ghost particle is formed from the same set of actual particles is found in both reconstructed volumes used in the 3D correlation analysis. Indeed, when the displacement normal to the viewing direction between two exposures is nearly equal for a given set of particle to approximately the particle image diameter, ghost particles are formed in both exposures and have a coherent. Their displacement is about the average velocity of the particle set responsible for the ghost

particle. This results in an underestimation of the displacement gradients. This phenomenon has a strong impact on the displacement field when the difference between particles along the volume depth is close to the particle image diameter. To illustrate this, Elsinga et al (2011) used a shear layer type displacement field in a 2D synthetic simulation,

$$(U,V) = (5 + \alpha z,0) \quad (8)$$

where α is a linear displacement gradient. They showed that for a small α gradient, the coherent motion of ghost particles strongly impacted the displacement field and that this phenomenon tends to disappear when α increases.

To determine FOLKI-3D behavior with respect to the coherent motion of ghost particles we performed 3D synthetic simulations, reconstructing particle distribution from 2D PIV images using a similar displacement field,

$$(U,V,W) = (\alpha z, 0, 0) \quad (9)$$

for α=0.01 and α=0.05 voxel/voxel. Estimated displacement fields can be assessed using the averaged norm of the error between estimated and ground truth displacement, defined as

$$VE_{gt} = \frac{1}{K}\sum_{k=1}^{K}\left\|\boldsymbol{v}(\boldsymbol{X}_k) - \boldsymbol{v}_{GT}(\boldsymbol{X}_k)\right\| \quad (10)$$

Here, v and v_{GT} respectively denote the estimated and ground truth displacements, and the index k identifies the grid points. It is also possible to base our quality measurement on the velocity $\mathbf{v}_{Ideal}$ estimated by using ideal reconstructions, as considered in section 3. In this case, the average Velocity Error is denoted VE_{Ideal}. The velocity overlap is chosen to be 75%, and the averaged velocity error is computed at points X_k which are included in a parallelepiped contained within the intersection volume of both the laser sheet and the cameras fields of view (Intersection) In order to achieve statistical convergence of this quantity, we performed the tests on typially three to five different initial particle distributions depending on the tests, each leading to different reconstructed volumes and velocity fields. In this section only top hat weighted interrogation volumes are considered. The interpolation scheme used is the cubic B-Spline, unless otherwise specified. The number of levels is J=3 and we used N=7 iterations.

4.2.2. Results

Fig. 4 shows displacement profiles along Z, averaged in the X and Y directions, for α=0.01 and α=0.05. Results are plotted for both an ideal particle distribution, and for reconstructed volumes from 2D images. We also compute the velocity of ghost particles by removing the real particles from the SMART reconstruction. The results show a clear underestimation of the displacement gradient for small α, similar to Elsinga et al. (2011), and this effect decreases as α increases. For α=0.05 both ideal and reconstructed mean displacement curves overlap. Elsinga et al. showed that this underestimation for small gradients is due to the coherent motion of ghost particles which appear in the reconstruction process, as a result of small displacement gradients orthogonal to the line of sight of the cameras.

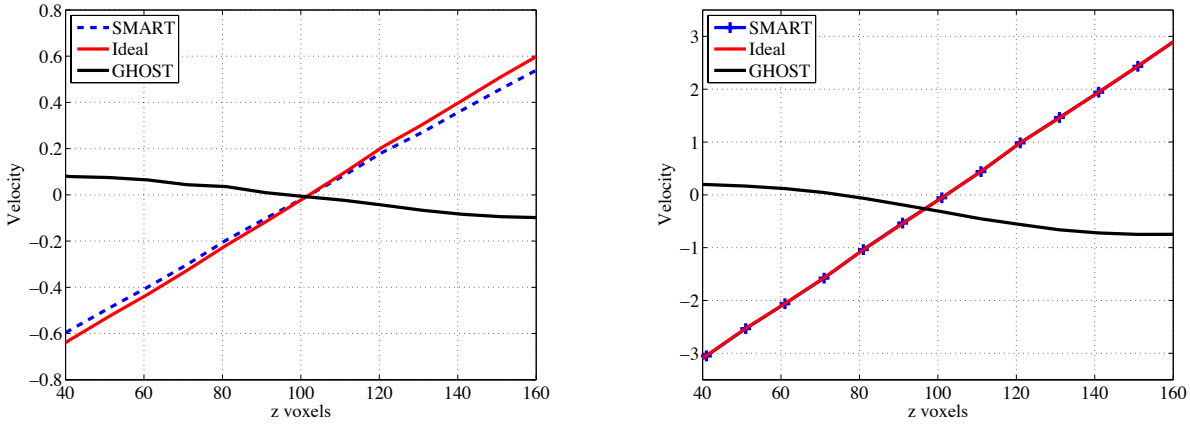

Fig. 4 Profiles along Z of the velocity averaged over X and Y for shear displacements with α=0.01 (left) and α=0.05 (right). Results showed here obtained with an IV side of 41 voxels (radius of 20 voxels).

Following Elsinga et al. 2006, Cheminet et al. (2013) and Cornic et al. 2013 further quantified the impact of 'added particles', i.e. particles that lie in the Union, as a source of noise on the reconstruction quality. To further understand the impact of this effect on the velocity measurement, we computed PIV images with particles only in the Intersection on the one hand, and particles in the Union on the other hand, and determined the displacements in the case of the α=0.01 shear displacement. **Fig. 5** shows the impact on the average velocity errors of particles which lie in the Union, but not in the Intersection, leading to a strong increase in the rms measurement errors (left figure). Indeed, those particles are responsible for an increase in the number of ghost particles in the reconstructed volume: the reconstruction quality Q (Elsinga 2006) for the Intersection case is 0.94 and drops to 0.79 for the Union case. **Fig. 5** (right) compares the average velocity profiles of the reconstruction and of the ghost particles in both cases. It is interesting to see that the ghost particles average velocity in the Union case is of opposite sign to the reconstruction velocity, thus impacting strongly the overall velocity estimation through a clear underestimation of the velocity gradient. These ghost particles lead to an increase in the rms errors as well as an increase in bias errors. To minimize their impact, experiments should thus be designed so as to maximize the ratio $R_{I/U}$ between Intersection and Union, as long as this does not increase other noise sources.

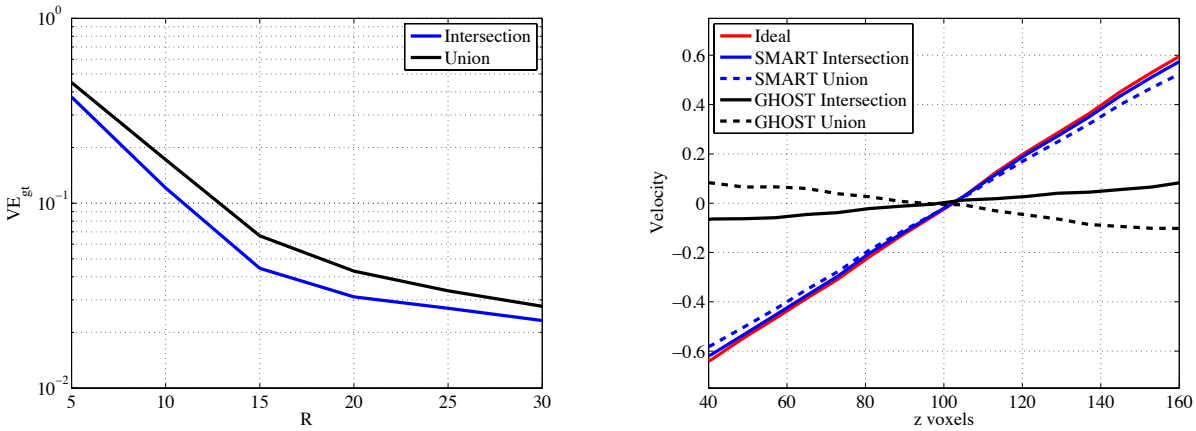

Fig. 5 Average velocity errors for α=0.01 (left) as a function of the IVs radius R. Velocity profiles along Z, averaged in the X and Y directions (right) for ideal reconstruction, SMART reconstruction and ghost particles. Cases where particles lie only in the Intersection, or in the Union. On the right subfigure, the IV side is set to 41 voxels (radius of 20 voxels).

In order to further situate FOLKI3D among other IDM algorithms, we performed a comparison with LaVision Davis 8.2, using the direct correlation setting, and with top hat interrogation volumes for both algorithms. Further parameters for Davis 8.2 include an intermediate rejection step using the universal outlier detection method (Westerweel et al. 2005), and smoothing between the iterations with a 3x3x3 Gaussian

filter. The test case chosen for this comparison is the α=0.01 shear displacement with illuminated particles lying in the Union volume, which was showed to be a particularly noisy case for the correlation. Firstly, we performed a tomographic reconstruction from the synthetic PIV images using our implementation of MLOS-SMART. Then, the same resulting reconstructed volumes were processed both by FOLKI3D and Davis. This operation was repeated with 3 different particles sets to achieve statistical convergence of the average velocity error. **Fig. 6** shows this quantity as well as the velocity profiles, for both algorithms.

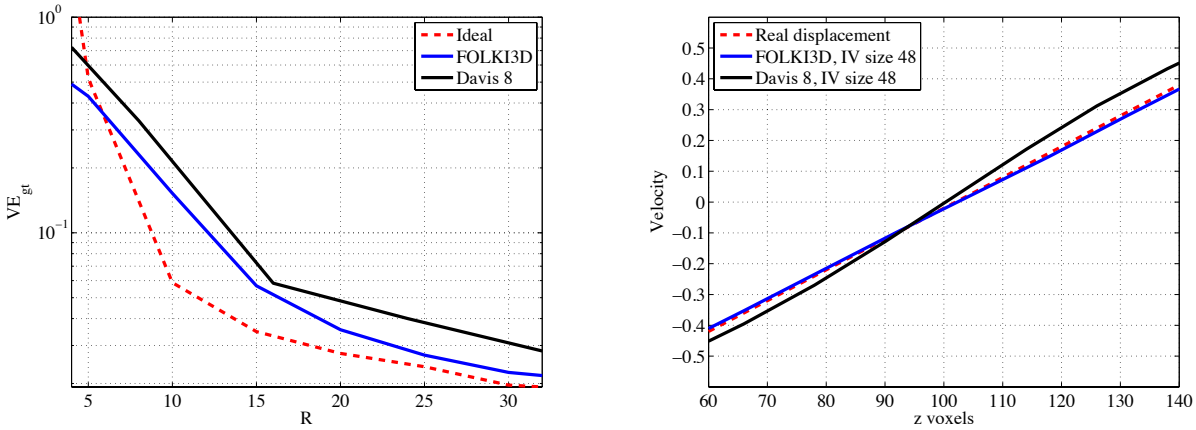

Fig. 6 Average velocity errors for α=0.01 (left) as a function of the IVs radius R, and velocity profiles along Z, averaged in the X and Y directions (with an IV side of 48 - radius of 24 voxel), obtained with FOLKI3D and Davis 8.2 on the same tomographic reconstructions, and with FOLKI3D on ideal volumic distributions.

In **Fig. 6**, FOLKI3D's rms displacement error VE_{gt} is compared to Davis's for different IVs sizes, and averaged velocity profiles are also compared for an IV side of 48 voxels. FOLKI3D and Davis have a similar behavior, the rms error rising as the IV size decreases. It turns out that FOLKI3D performs equally or better than Davis whereas it does not involve any data post-processing between two successive iterations. This is especially true for small IV sizes. Champagnat et al. (2011) showed the same results on the 2D version of the algorithm.

4.3. Interpolators and shape of the reconstructed particles

As studied by Elsinga et al. (2006) and Scarano (2013) among others, the reconstruction quality is strongly dependent on the global aperture angle of the cameras. Indeed, small values of the aperture will lead to reconstructed particles with an elongated shape in the Z direction, whereas larger apertures will allow to obtain more isotropic blobs. In this section, we further consider the impact of this parameter on the corresponding velocity fields, and also investigate the influence on the result of the interpolation scheme used during deformation. We choose a camera arrangement in the form of a cross (or '+' sign), parameterized by its aperture angle β, similar to that considered in Scarano (2013), and vary β between 20 and 100°. For each angle value, as in the previous sections, we generate two sets of synthetic images, corresponding to particles lying either in the Intersection only, or in the Union. Note that, since the voxel-to-pixel ratio is chosen equal to 1 in all situations, choosing the same ppv for all angles results in images with the same ppp. Thus, varying the angle β will amount to varying the Intersection to Union ratio $R_{I/U}$, thereby varying the proportion of ghosts, as well as the shape of the reconstructed particles.

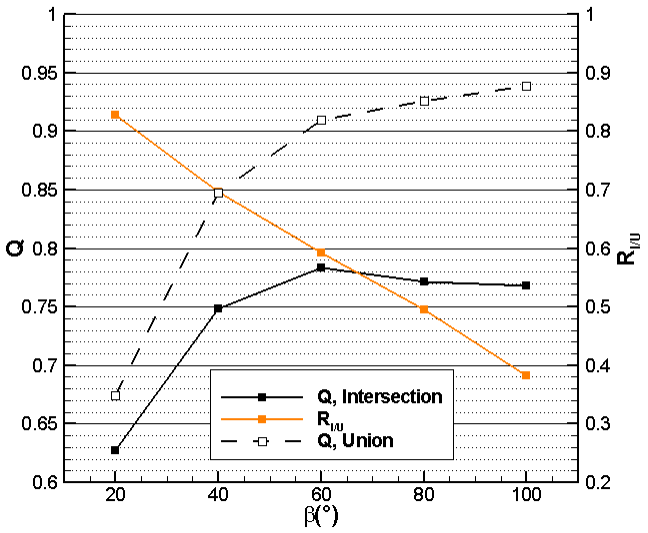

Fig. 7 Reconstruction quality as a function of the camera aperture angle β, for synthetic images generated with particles contained only in the Intersection, or in the Union. The value of the Intersection to Union ratio $R_{I/U}$ is also indicated.

Fig. 7 shows the evolution of the reconstruction quality as a function of β in the Intersection and Union cases. Similarly to Scarano (2013), one logically observes an important drop in Q for decreasing β, due to the elongation of the reconstructed particles in the Z direction. In the realistic Union case, the quality does not increase strictly with β contrary to the Intersection case, but reaches a plateau from $\beta \approx 60°$, close to a 0.75-0.8 level. This is due to the fact that as β increases, the $R_{I/U}$ ratio increases. Therefore, even if the shape of the reconstructed particles is closer to ideal, the corresponding gain in quality is cancelled by an increase in the number of ghosts due to added particles.

In **Fig. 8**, the corresponding displacement rms errors are represented separately for each component, for fields obtained using either the linear or the cubic B-Spline interpolators in FOLKI3D. In all cases, the IV size has been set to 41 voxels. The ground truth displacement considered here is made up of the superposition of shearing motions along both U and W, with the same strength $\alpha = 0.01$. More precisely:

$$(U,V,W) = (\alpha Z, 0, \alpha X) \quad (11)$$

The resulting velocity field is thus a hyperbolic point in the XZ plane. Starting with the Intersection case (left subfigure), one observes that, logically, the rms error on W explodes for the smaller value of β and becomes comparable to that on U and V for values equal or larger to 40°. Another important result is that fields with the B-Spline interpolator have quasi-systematically lower rms errors than with the linear interpolator for all components. The exception is precisely the rms error on W for the smaller values of β. However, these angles correspond to small apertures, which are rarely considered in practice, as they have a large rms error also with the linear interpolator. Therefore, it can be concluded that in a more complex situation than the ideal distribution considered in section 3.2 (that is, actual reconstructions with noise in the images), the use of a B-Spline interpolator for deformation allows a significant increase in the accuracy. Going one step further in complexity, when particles lie in the Union field (right subfigure), one observes that this gain is robust, with overall comparable results for both interpolators. A slight difference is observed, in the form of higher rms values for all components and interpolators for the largest values of β (80 and 100°). This can be probably be ascribed to the large number of ghost particles due to the low value of the $R_{I/U}$ ratio.

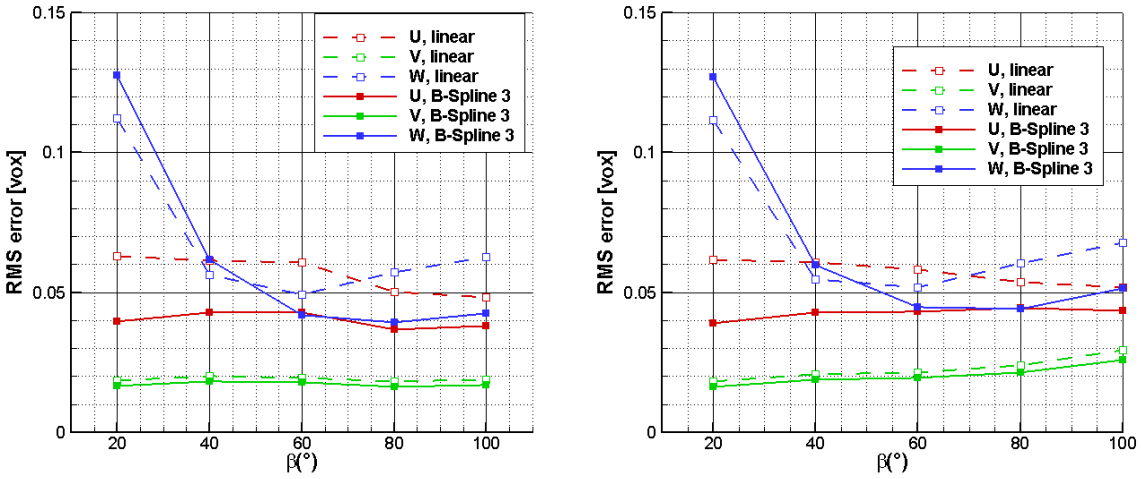

Fig. 8 Componentwise RMS error for linear and cubic B-Spline interpolators as a function of the camera aperture angle β, for synthetic images generated with particles contained only in the Intersection (left), or in the Union (right). The displacement field is a shearing motion with α=0.01, as in section 4. The IV size in FOLKI3D is of 41 voxels (radius of 20)

Conclusion

An extension to 3D of the algorithm FOLKI-PIV (Champagnat et al. 2011) has been introduced. As in the planar context, the displacement is searched as the minimizer of a sum of squared differences, which is solved iteratively by using volume deformation. The latter may be performed using a simple, linear scheme or a higher-order, cubic B-Spline scheme. Tests performed on synthetic 3D particle distributions have confirmed that the spatial frequency response is similar to that of standard iterative deformation algorithms, for both top-hat and Gaussian weightings, while similar gains as reported in the literature are obtained by choosing the cubic B-Spline interpolation rather than the linear one. Tests on volumes reconstructed from projected images have then allowed to characterize the robustness of the algorithm to specific tomographic noise (i.e., ghost particles), as well as the gain brought by the higher-order interpolation in a more realistic configuration. FOLKI3D has been found in particular more robust to coherent ghosts, while the gain in accuracy of the high-order deformation has been confirmed for various quantities of ghosts in the reconstructions, and various shapes of the reconstructed particles.

In future works, we will pursue these tests by considering more complex displacement fields, as well as experimental data on a cylindrical jet, in order to evaluate the potential of FOLKI3D to the study of 3D turbulent flows. The algorithmic optimization will also be continued, firstly in order to reach the most efficient computational times within the present algorithm, and then in order to include more advanced methods, such as time-resolved, for instance.

References

1. Atkinson C., Soria J., An efficient simultaneous reconstruction technique for tomographic particle image velocimetry. Exp. in Fluids 47 (2009): 553–568.
2. Astarita T., Cardone G., Analysis of interpolation schemes for image deformation methods in PIV, Exp. Fluids 38, 2005.
3. Baker S., Matthews I., Lucas-Kanade 20 years on: a unifying framework, Int. J. Comput. Vis. 61(3), 2004.
4. Champagnat F., Plyer A., Le Besnerais G., Leclaire B., Davoust S., Le Sant Y., Fast and accurate PIV computation using a highly parallel iterative correlation maximization, Exp. Fluids (2011) 50:1169-1182
5. Champagnat F., Le Sant Y., Efficient cubic B-Spline image interpolation on a GPU, J. Graphics Tools 16(4), 2013.
6. Cheminet A., Leclaire B., Champagnat F., Cornic P., Le Besnerais G. (2013). On factors affecting the

quality of tomographic reconstruction, in 'Proceedings of PIV13'.
7. Cornic P., Champagnat F., Cheminet A., Leclaire B., Le Besnerais G. (2013). Computationally efficient sparse algorithms for tomographic PIV reconstruction, in 'Proceedings of PIV13'
8. Elsinga G., Scarano F., Wieneke B., Van Oudheusden B., Tomographic particle image velocimetry, Exp. Fluids 41, 2006.
9. Elsinga G., Westerweel J., Scarano F., Novara M., On the velocity of ghost particles and the bias errors in Tomographic-PIV, Exp. Fluids 50, 2011.
10. Leclaire B., Le Sant Y., Le Besnerais G., Champagnat F., On the stability and spatial resolution of image deformation PIV methods, 9th Int Symp on Particle Image Velocimetry - PIV11, Kobe, Japan, July 21-23, 2011.
11. Scarano F., Tomographic PIV: principles and practice, Meas. Sci. Technol. 24, 2013.
12. Scarano F., Riethmuller M., Advances in iterative multigrid PIV image processing, Exp. Fluids 29(1), 2000.
13. Schrijer F., Scarano F., Effect of predictor-corrector filtering on the stability and spatial resolution of iterative PIV interrogation, Exp. Fluids 45, 2008.
14. Stanislas M., Okamoto K., Kähler C., Westerweel J., Scarano F., Main results of the third international PIV challenge, Exp. Fluids 45, 2008.
15. Westerweel J., Scarano F., Universal outlier detection for PIV data, Exp. Fluids 39, 2005 : 1096-1110